

Reverberation Mapping of the Broad-line Region in NGC 5548: Evidence for Radiation Pressure?

Kai-Xing Lu^{1,2}, Pu Du², Chen Hu², Yan-Rong Li², Zhi-Xiang Zhang², Kai Wang², Ying-Ke Huang², Shao-Lan Bi¹, Jin-Ming Bai³, Luis C. Ho^{4,5} and Jian-Min Wang^{2,6,*}

ABSTRACT

NGC 5548 is the best-observed reverberation-mapped active galactic nucleus with long-term, intensive monitoring. Here we report results from a new observational campaign between January and July, 2015. We measure the centroid time lag of the broad $H\beta$ emission line with respect to the 5100 Å continuum and obtain $\tau_{\text{cent}} = 7.20^{+1.33}_{-0.35}$ days in the rest frame. This yields a black hole mass of $M_{\bullet} = 8.71^{+3.21}_{-2.61} \times 10^7 M_{\odot}$ using a broad $H\beta$ line dispersion of $3124 \pm 302 \text{ km s}^{-1}$ and a virial factor of $f_{\text{BLR}} = 6.3 \pm 1.5$ for the broad-line region (BLR), consistent with the mass measurements from previous $H\beta$ campaigns. The high-quality data allow us to construct a velocity-binned delay map for the broad $H\beta$ line, which shows a symmetric response pattern around the line center, a plausible kinematic signature of virialized motion of the BLR. Combining all the available measurements of $H\beta$ time lags and the associated mean 5100 Å luminosities over 18 campaigns between 1989 and 2015, we find that the $H\beta$ BLR size varies with the mean optical luminosity, but, interestingly, with a possible delay of $2.35^{+3.47}_{-1.25}$ yrs. This delay coincides with the typical BLR dynamical timescale of NGC 5548, indicating that the BLR undergoes dynamical changes, possibly driven by radiation pressure.

Subject headings: galaxies: active—galaxies: individual (NGC 5548)—galaxies: nuclei

1. Introduction

Reverberation mapping (RM) is a powerful tool to probe the geometry and structure of broad-line regions (BLRs) in active galactic nuclei (AGNs) (Bahcall et al. 1972; Blandford & McKee 1982;

¹Department of Astronomy, Beijing Normal University, Beijing 100875, China

²Key Laboratory for Particle Astrophysics, Institute of High Energy Physics, Chinese Academy of Sciences, 19B Yuquan Road, Beijing 100049, China.

³Yunnan Observatory, Chinese Academy of Sciences, Kunming 650011, Yunnan, China.

⁴Kavli Institute for Astronomy and Astrophysics, Peking University, Beijing 100871, China

⁵Department of Astronomy, School of Physics, Peking University, Beijing 100871, China

⁶National Astronomical Observatories of China, Chinese Academy of Sciences, 20A Datun Road, Beijing 100020, China

*Corresponding author: wangjm@ihep.ac.cn

Peterson 1993). Over the past four decades, great efforts on RM monitoring have yielded a precious sample of ~ 60 nearby Seyfert galaxies and quasars with measurements of $H\beta$ time lags (e.g., Bentz et al. 2013; Du et al. 2016a), among them NGC 5548, the best-observed source that has been intensively monitored by 17 individual RM campaigns, including the recent Space Telescope and Optical Reverberation Mapping Project (AGN STORM; De Rosa et al. 2015; Edelson et al. 2015; Fausnaugh et al. 2015; see Peterson et al. 2002 for a summary of the first 13 campaigns; Bentz et al. 2007, 2009). NGC 5548 therefore serves as a valuable laboratory to study in detail the long-term variations of the BLR (Wanders & Peterson 1996; Sergeev et al. 2007), as well as the consistency and reliability of RM-based black hole (BH) mass measurements (Peterson et al. 1999; Collin et al. 2006).

NGC 5548 follows the relation $R_{\text{BLR}} \propto L_{5100}^{0.79 \pm 0.2}$ (Kilerci Eser et al. 2015), where L_{5100} is the optical luminosity at 5100 Å. This relation for NGC 5548 is significantly different from the well-known radius–luminosity relation $R_{\text{BLR}} \propto L_{5100}^{0.53 \pm 0.04}$ for the overall RM sample (Kaspi et al. 2000; Bentz et al. 2013). This difference needs to be understood. On the other hand, the geometry and kinematics of the BLR in NGC 5548 have been investigated by velocity-resolved mapping in several studies (e.g., Denney et al. 2009b; Bentz et al. 2010; De Rosa et al. 2015), and by recently developed dynamical modelling (Pancoast et al. 2014b) using the data taken by the 2008 Lick AGN Monitoring Project (LAMP; Bentz et al. 2009). However, the inferred BLR dynamics seems diverse, and there is no consensus¹.

To investigate the above issues, we conducted a new observational campaign for NGC 5548 in 2015. This paper presents the results of our new RM campaign. In Section 2, we describe the observations and the data reduction in detail. In Section 3, we perform the time series analysis and measure the $H\beta$ time lags and construct the velocity-resolved lags of the broad $H\beta$ line. We investigate the structure and dynamics of the BLR in Section 4, and discuss the BH mass measurements, accretion rates, and the long-term variations of BLR size in Section 5. We draw our conclusions in Section 6. Throughout the paper, a cosmology with $H_0 = 67 \text{ km s}^{-1} \text{ Mpc}^{-1}$, $\Omega_{\Lambda} = 0.68$, and $\Omega_{\text{M}} = 0.32$ is adopted (Ade et al. 2014).

2. Observations and Data Reduction

2.1. Observations

The spectroscopic and photometric observations of NGC 5548 were made using the Yunnan Faint Object Spectrograph and Camera (YFOSC), mounted on the Lijiang 2.4 m telescope at

¹This can be seen by comparing Figure 3 from Denney et al. (2009b) with Figure 19 from Bentz et al. (2010), who present observations from 2007 and 2008, respectively. Such a difference cannot be caused by intrinsic variations of the BLR because the time separation between the two campaigns is significantly shorter than the BLR dynamical timescale (see Equation 9).

Yunnan Observatory, Chinese Academy of Sciences. Working at the Cassegrain focus, YFOSC is a versatile instrument for low-resolution spectroscopy and photometry. It is equipped with a back-illuminated 2048×2048 pixel CCD, with pixel size $13.5 \mu\text{m}$, pixel scale $0.283''$ per pixel, and field-of-view $10' \times 10'$. YFOSC can automatically switch from spectroscopy to photometry within 1 s (see [Du et al. 2014](#)).

Our observations started on January 7, 2015 and ended on July 11, 2015. To get an accurate flux calibration, we simultaneously observed a nearby comparison star along the long-slit as a reference standard. Such an observation strategy was described in detail by [Maoz et al. \(1990\)](#) and [Kaspi et al. \(2000\)](#), and was recently adopted by [Du et al. \(2014\)](#). As shown in Figure 1, we chose the star labeled “No.1” as the comparison star. Given the seeing of $1.0'' - 2.5''$ throughout the monitoring period, we fixed the projected slit width at $2.5''$. We used Grism 14, which provides a resolution of 92 \AA mm^{-1} ($1.8 \text{ \AA pixel}^{-1}$) and covers the wavelength range $3800 - 7200 \text{ \AA}$. Standard neon and helium lamps were used for wavelength calibration. To reduce atmospheric differential refraction, we limited the observations to airmasses $\lesssim 1.2$. This guarantees an atmospheric refraction $\leq 0.3''$ over the wavelength range $4500 - 5500 \text{ \AA}$ ([Filippenko 1982](#)). The mean airmass for all the spectra is 1.07, so that any offset of the target from the slit center due to atmospheric refraction is limited to $\lesssim 0.14'' - 0.21''$, which has a negligible impact on our analysis.

To verify the calibration of the spectroscopic data, we also made photometric observations using a Johnson *V* filter. We took three consecutive exposures of 90 s each. In total, we obtained 62 spectroscopic observations and 61 photometric observations, spanning a time period of 180 days. The typical cadence is ~ 3.4 days.

2.2. Data Reduction

The two-dimensional spectroscopic images were reduced using the standard IRAF tools before absolute flux calibration. This includes bias subtraction, flat-field correction, and wavelength calibration. All the spectra were extracted using a uniform aperture of 30 pixels ($8.5''$), and the background was determined from two adjacent regions on either side of the aperture region. As described in [Du et al. \(2014\)](#), absolute flux calibration was done in two steps. (1) The observations taken during nights with good weather conditions were used to calibrate the absolute flux of the comparison star, which was then used as the fiducial spectrum for absolute flux standard for the science observations. (2) For each object/comparison star pair, a wavelength-dependent sensitivity function was obtained by comparing the star’s spectrum to the fiducial spectrum. Then this sensitivity function was applied to calibrate the observed spectrum of the target. The spectra calibrated in this way show a small fluctuation of the $[\text{O III}] \lambda 5007$ flux at a level of 2%, which can be regarded as the accuracy of our absolute flux calibration.

The *V*-band images were also reduced using standard IRAF (V2.16) procedures. Instrumental magnitudes were measured with respect to five selected reference stars in the field (see Figure 1).

The typical accuracy of the photometry is 0.015 mag.

2.3. Spectral Measurements

Following [Hu et al. \(2015\)](#), we measured the 5100 Å continuum and broad H β line using a spectral fitting scheme. The fitting components include (1) a single power-law continuum; (2) a stellar component for the host galaxy; (3) Fe II emission; (4) broad H β emission line; (5) broad He II λ 4686 emission line; and (6) narrow emission lines of [O III] λ 4959, 5007, He II λ 4686, H β , and several coronal lines (such as [Fe VII] λ 5158, [Fe VI] λ 5176 and [Ca V] λ 5309; see the details in [Hu et al. 2015](#)). The spectral template for the host galaxy is a stellar population model with an age of 11 Gyr and a metallicity $Z = 0.05$ [Bruzual & Charlot 2003](#).

During the observations, seeing variations and mis-centering of the object in the slit lead to varying amounts of host galaxy light in the final spectrum. To remove this effect, the flux of the host galaxy component is set to a free parameter in our fitting scheme. During the whole monitoring period, the H β emission line of NGC 5548 showed extreme broad wings, in addition to a strong narrow component. We slightly modified the fitting scheme of [Hu et al. \(2015\)](#) in two aspects, by adding a narrow component to H β and using three Gaussians to fit the broad component. Figure 2 shows the fitting results for the mean spectrum of our campaign and for an individual spectrum.

We measured the 5100 Å continuum from the best-fit power-law component and the H β flux by integrating the best-fit broad components of H β from 4710 Å to 5050 Å. For the purpose of constructing the velocity-resolved delay map (see Section 3.3), we obtained the broad H β profile by subtracting the host galaxy, Fe II and [O III] emission lines, and the narrow component of H β . Table 1 summarizes the light curves. Figure 3 plots the light curves of the V-band photometry (instrumental magnitude in an arbitrary unit), 5100 Å continuum, and broad H β flux.

3. Time Series Analysis

3.1. Variability Characteristics

Following standard practice (e.g., [Rodríguez-Pascual et al. 1997](#)), we calculate the variability amplitude of the light curves of the 5100 Å continuum and H β emission line by

$$F_{\text{var}} = \frac{(\sigma^2 - \Delta^2)^{1/2}}{\langle F \rangle} \quad (1)$$

and its uncertainty ([Edelson et al. 2002](#))

$$\sigma_{F_{\text{var}}} = \frac{1}{F_{\text{var}}} \left(\frac{1}{2N} \right)^{1/2} \frac{\sigma^2}{\langle F \rangle}, \quad (2)$$

where $\langle F \rangle = N^{-1} \sum_{i=1}^N F_i$ is the average flux, F_i is the flux of the i -th observation of the light curve, N is the total number of observations, $\sigma^2 = \sum_{i=1}^N (F_i - \langle F \rangle)^2 / (N - 1)$, $\Delta^2 = \sum_{i=1}^N \Delta_i^2 / N$, and Δ_i is the uncertainty of F_i . Table 2 lists the statistics of the light curves. The variability amplitudes of the 5100 Å continuum and broad H β line are $F_{\text{var}} = 0.23$ and 0.10, respectively, which are generally comparable with those of previous RM campaigns, after correcting for host galaxy and narrow H β contributions (Peterson et al. 2002; Bentz et al. 2007; Denney et al. 2010). We also calculate another standard measure of variability, R_{max} , simply defined by the ratio of maximum to minimum flux. The values of R_{max} are 2.31 and 1.52 for the 5100 Å continuum and broad H β line, respectively.

3.2. H β Time Lags

We compute the time lag of H β line flux relative to 5100 Å continuum using the interpolation cross-correlation function method (ICCF; Gaskell & Sparke 1986; Gaskell & Peterson 1987; White & Peterson 1994). The time lag is measured by two standard approaches: the peak location τ_{peak} of the ICCF (r_{max}) and the centroid τ_{cent} of the ICCF around the peak above a typical value ($r \geq 0.8 r_{\text{max}}$). Their respective uncertainties were obtained using the Monte Carlo “flux randomization/random subset sampling” method described by Peterson et al. (1998) and Peterson et al. (2004). The Monte Carlo simulations were run with 1000 realizations, and the distributions of the peak and centroid (CCPD and CCCD) were created from the generated samples. The uncertainties of τ_{peak} and τ_{cent} are then calculated from the CCPD and CCCD, respectively, with a 68.3% confidence level (1σ).

In Figures 3(d) and 3(e), we show the auto cross-correlation function (ACF) of the light curve of 5100 Å continuum, the ICCF between the H β flux and 5100 Å continuum, and the CCPD and CCCD of the ICCF, respectively. We find that the ICCF peak occurs at $\tau_{\text{peak}} = 7.20^{+1.33}_{-0.35}$ days ($r_{\text{max}} = 0.83$) and the ICCF centroid occurs at $\tau_{\text{cent}} = 7.18^{+1.38}_{-0.70}$ days in the rest frame (see Table 3). As an independent check, we also calculate the Z-transformed discrete correlation function (ZDCF; Edelson & Krolik 1988; Alexander 1997) and superpose the corresponding ZDCF in Figures 3(d) and 3(e). As can be seen, the ZDCFs are in good agreement with the ICCFs.

3.3. Velocity-resolved Reverberation Mapping

Velocity-resolved RM is widely used to reveal the kinematic signatures of BLRs (e.g., Grier et al. 2013; Bentz et al. 2008, Bentz et al. 2010; Denney et al. 2009a,b, 2010; De Rosa et al. 2015; Du et al. 2016b). The high-quality spectroscopic data of our campaign allow us to construct the velocity-binned delay map of the H β line. Our procedure is as follows. Using the method described in the Appendix, we first calculate the RMS spectrum of the broad H β profiles obtained in Section 2.3. As illustrated in Figure 4(a), we then select a wavelength range from 4731 Å to 4991 Å in the rest

frame and divide the $H\beta$ profiles into nine uniformly spaced bins (each bin has a velocity width of $\sim 1700 \text{ km s}^{-1}$)². The light curve of each bin is finally obtained by just integrating the flux in the bin. The time lag of each bin and the associated uncertainties are determined using the same procedures as described in Section 3.2.

In Figure 5, we plot the obtained light curves of the nine bins, along with the light curve of the 5100 Å continuum for the sake of comparison. The corresponding ICCFs between the light curve of each bin and the continuum are shown in the right panels of Figure 5, in which the CCCD and CCPD are also superposed. The velocity-resolved delay map is plotted in Figure 4(b). We can find that the delay map has a symmetric pattern, with longer response at the line core and shorter response at the wings (except for bin 5).

Velocity-resolved delay maps of the broad $H\beta$ line in NGC 5548 were derived previously in the MDM campaign undertaken in 2007 (Denney et al. 2009a,b) and in the LAMP campaign in 2008 (Bentz et al. 2009). The delay map of our campaign is very similar to that of the MDM campaign. Denney et al. (2009a) conclude that the symmetric delay map of NGC 5548 indicates that there is no radial gas motion in the BLR. The data quality of the LAMP campaign is relatively poor so that the resulting delay map in Bentz et al. (2009) does not reveal clear signatures for the BLR motion. However, Pancoast et al. (2014b) carried out dynamical modeling of the LAMP data and found that a narrow thick-disk-like BLR geometry with dominant inflows can explain the variations of the broad $H\beta$ line. On the other hand, it is worth mentioning that the C IV velocity-resolved delay map of the AGN STORM campaign derived by De Rosa et al. (2015) shows a symmetric structure. In the future, detailed analysis of the present data through dynamical modeling (e.g., Pancoast et al. 2011; Li et al. 2013) will better constrain the kinematics of the $H\beta$ BLR.

4. Structure and Dynamics of the BLR

This section examines the virial assumption for the BLR motions and the relation between the $H\beta$ BLR size and optical luminosity, by combining data from all the available RM campaigns of NGC 5548. We compile the width and time lags of $H\beta$ from the literature (Peterson et al. 2004; Collin et al. 2006; Bentz et al. 2007; Denney et al. 2010; Bentz et al. 2010; Fausnaugh et al. 2015). Kilerci Eser et al. (2015) re-calibrated the 5100 Å flux using the updated flux measurements of the host galaxy given in Bentz et al. (2013). We directly take these re-calibrated fluxes to calculate the 5100 Å luminosity. Table 4 summarizes all the RM measurements of $H\beta$ lag, $H\beta$ flux, and the dispersion and full width half maximum (FWHM) velocity of the $H\beta$ line from RMS and mean spectra.

²It should be pointed out that the instrumental broadening is about 500 km s^{-1} for the $2.5''$ slit, significantly smaller than the width of the velocity bin. We thus did not employ the method of Du et al. (2016b) to correct the spectra for instrumental broadening.

4.1. The Virial Relation

We employ the method of [Peterson et al. \(2004\)](#) to measure the FWHM and σ_{line} of $\text{H}\beta$ from the mean and RMS spectra (Table 3; Appendix). We find $\text{FWHM}/\sigma_{\text{line}} \approx 3$, which is larger than 2.35 for a Gaussian profile, indicating that the BLR has less turbulent motion ([Kollatschny & Zetzl 2013](#)). We calculate the virial product (Table 4)

$$\text{VP} = \frac{c\tau_{\text{H}\beta}V^2}{G}, \quad (3)$$

where $\tau_{\text{H}\beta}$ is the $\text{H}\beta$ time lag, c is the speed of light, G is the gravitational constant, and V is the line width. If the BLR motion is dominated by the gravity of the central BH and is virialized, VP should be constant, and $V \propto \tau_{\text{H}\beta}^{-1/2}$.

Figure 6 shows the relation between V and $\tau_{\text{H}\beta}$ using four measures of line width, namely σ_{line} and FWHM from the mean and RMS spectra. The relations between V and $\tau_{\text{H}\beta}$ have a slope of $(-0.54, -0.55, -0.55, -0.40)$ for σ_{line} and FWHM of the RMS and mean spectra, respectively. Generally, the $\text{H}\beta$ line width obeys the virial relation within the uncertainties, consistent with the results reported by [Peterson et al. \(2004\)](#) and [Bentz et al. \(2007\)](#). To quantitatively describe any deviation of the BLR motion from the virial relation, we define a parameter

$$\delta = \sum_i^N \delta_{V_i}^2, \quad \text{and} \quad \delta_{V_i} = \log \left(\frac{V_i}{V_{\text{vir}}} \right), \quad (4)$$

where $V_{\text{vir}} = (G\langle\text{VP}\rangle/R_{\text{BLR}})^{1/2}$ and $\langle\text{VP}\rangle$ is the average virial product. We find that the deviation $\delta = (0.11, 0.10, 0.10, 0.19)$ for σ_{line} and FWHM of the RMS and mean spectra, respectively.

4.2. The VP and 5100 Å Luminosity

Figures 7(a) and (b) show the distribution of VP as a function of optical luminosity. Compared with the previous analysis of [Collin et al. \(2006\)](#) and [Bentz et al. \(2007\)](#), we extend the analysis by including the latest RM measurements. Using the procedure FITEXY of [Press et al. \(1992\)](#), we obtain the regressions

$$\log(\text{VP}/M_{\odot}) = \begin{cases} (7.13 \pm 0.04) + (0.21 \pm 0.13) \log \ell_{43} & (\text{for } \sigma_{\text{line}}), \\ (7.97 \pm 0.05) + (0.36 \pm 0.20) \log \ell_{43} & (\text{for FWHM}), \end{cases} \quad (5)$$

where $\ell_{43} = \bar{L}_{5100}/10^{43} \text{ erg s}^{-1}$. Figures 7(c) and (d) show that the distributions of $\text{VP}|_{\sigma_{\text{line}}}$ and $\text{VP}|_{\text{FWHM}}$ have a large scatter (0.31 and 0.32 dex, respectively). We note that the weak correlation between VP and luminosity is not in conflict with the notion that the BLR is predominantly virialized. Even if variations in radiation pressure induces secular departures from virial equilibrium, the kinematics gradually adjusts to restore a quasi-virialized state. This test shows that the method for determining the BH mass is robust as long as the factor f_{BLR} is reliably calibrated.

4.3. The BLR Radius–Luminosity Relation

Peterson et al. (2004) found that the $R_{\text{BLR}} - \bar{L}_{5100}$ relation of NGC 5548 has a much steeper slope than 0.5. Figure 8(a) reemphasises this point, by including the new measurement from our campaign. Using FITEXY, we obtain the best-fit regression of

$$\log(R_{\text{H}\beta}/\text{lt d}) = (0.94 \pm 0.05) + (0.86 \pm 0.18) \log \ell_{43}, \quad (6)$$

where $\ell_{43} = \bar{L}_{5100}/10^{43} \text{ erg s}^{-1}$. With the addition of the new data, our derived relation is slightly steeper than that reported by Kilerci Eser et al. (2015; $R_{\text{BLR}} \propto L_{5100}^{0.79 \pm 0.2}$). Both slopes are steeper than the value of 0.5 expected from simple photoionization theory. For completeness, Figure 8(b) also shows the best-fit regression of the relation between the H β BLR size and the H β luminosity, $R_{\text{H}\beta} \propto \bar{L}_{\text{H}\beta}^{0.87 \pm 0.25}$. Recently, based on data from simultaneous optical and UV observations, Kilerci Eser et al. (2015) established the connection between the 5100 Å and the 1350 Å luminosity, as $\bar{L}_{5100} \propto \bar{L}_{1350}^{0.63 \pm 0.12}$. Using this relation, we deduce $R_{\text{H}\beta} \propto \bar{L}_{1350}^{0.54 \pm 0.22}$, which is consistent with the expected slope of 0.5. This non-linear relation between the optical and UV emissions implies a complicated geometry for the accretion disk and the importance of radiative reprocessing (e.g., Fausnaugh et al. 2015; Edelson et al. 2015).

5. Discussion

5.1. Black Hole Mass and Accretion Rate

Following standard practice, we estimate the BH mass as

$$M_{\bullet} = f_{\text{BLR}} \frac{c\tau_{\text{H}\beta} V^2}{G}, \quad (7)$$

where f_{BLR} is a coefficient that crudely accounts for the unknown inclination, geometry, and kinematics of the BLR. Ho & Kim (2014) point out that the BLR in pseudobulges notably has a lower f_{BLR} than in classical bulges. For line dispersion σ_{line} measured from RMS spectra, $f_{\text{BLR}} = 3.2 \pm 0.7$ for pseudobulges, whereas $f_{\text{BLR}} = 6.3 \pm 1.5$ for classical bulges. The latter is roughly consistent, within uncertainties, with previous calibrations that do not take the bulge type into consideration (e.g., $f_{\text{BLR}} = 5.5 \pm 1.7$; Onken et al. 2004). NGC 5548 hosts a classical bulge (Ho & Kim 2014). Using $f_{\text{BLR}} = 6.3 \pm 1.5$, we derive a BH mass of $M_{\bullet}|\sigma_{\text{line}} = 8.71^{+3.21}_{-2.61} \times 10^7 M_{\odot}$; line dispersion measured from mean spectra, $f_{\text{BLR}} = 5.6 \pm 1.3$ (Ho & Kim 2014) and $M_{\bullet}|\sigma_{\text{line}} = 8.91^{+3.08}_{-2.67} \times 10^7 M_{\odot}$. The two mass measurements are in good agreement. Meanwhile, our measurements are also consistent, within the uncertainties, with the overall values from previous RM campaigns. A notable exception is the work of Pancoast et al. (2014b); applying the BLR dynamical modeling developed by Pancoast et al. (2014a) to the LAMP data on NGC 5548, they obtain, without invoking the virial factor, $M_{\bullet} = 3.89^{+2.87}_{-1.49} \times 10^7 M_{\odot}$, which is only about half of the virial-based value.

The classical bulge of NGC 5548 has a central stellar velocity dispersion of $\sigma_* = 195 \pm 13$ km s^{−1} (Woo et al. 2010), resulting in $M_\bullet|_{\sigma_*} = (2.75 \pm 0.88) \times 10^8 M_\odot$ from the latest $M_\bullet - \sigma_*$ relation (Kormendy & Ho 2013). This is marginally larger than the virial-based BH mass estimate, after taking into account the intrinsic scatter of the virial factor (Ho & Kim 2014), but significantly exceeds the BH mass determination based on dynamical modeling of the BLR by Pancoast et al. (2014b).

With the BH mass in hand, we can calculate the dimensionless accretion rate, defined as

$$\dot{\mathcal{M}} = \frac{\dot{M}_\bullet c^2}{L_{\text{Edd}}} \approx 0.1 \eta_{0.1}^{-1} \left(\frac{L_{\text{bol}}}{10^{44} \text{ erg s}^{-1}} \right) \left(\frac{M_\bullet}{10^8 M_\odot} \right)^{-1}, \quad (8)$$

where \dot{M}_\bullet is the mass accretion rate, $L_{\text{Edd}} = 1.5 \times 10^{38} (M_\bullet/M_\odot) \text{ erg s}^{-1}$ is the Eddington luminosity, $L_{\text{bol}} = \eta \dot{M}_\bullet c^2$ is the bolometric luminosity (see Table 5), and $\eta_{0.1} = \eta/0.1$ is the radiative efficiency of the accretion disk. Using a BH mass of $M_\bullet = 8.71 \times 10^7 M_\odot$ and a mean bolometric luminosity of $L_{\text{bol}} = 10^{44.33} \text{ erg s}^{-1}$ (Table 5), we obtain $\dot{\mathcal{M}} = 0.21$ for $\eta = 0.1$. The BH in NGC 5548 has an accretion rate in the regime of the standard accretion disk model (Shakura & Sunyaev 1973). Note that the above accretion rate is inaccurate if NGC 5548 hosts a binary supermassive BH, as recently suggested by Li et al. (2016) based on the detection of periodic variations in luminosity and velocity.

5.2. Potential Explanation: Radiation Pressure?

Figure 9 shows the variations of the mean \bar{L}_{5100} and R_{BLR} over all the 18 campaigns since 1989. The variation amplitude of \bar{L}_{5100} exceeds an order of magnitude. The lowest $L_{5100} \sim 10^{42.2} \text{ erg s}^{-1}$ occurred in 2005–2009 (Bentz et al. 2007; Bentz et al. 2009; Denney et al. 2010) and the highest $L_{5100} \sim 10^{43.5} \text{ erg s}^{-1}$ in 1998–1999 (Peterson et al. 1999; Peterson et al. 2002). Meanwhile, R_{BLR} also exhibits large variations, from ~ 5 up to ~ 30 light-days. Simple inspection of Figure 9 reveals that the changes in R_{BLR} follow the variations of \bar{L}_{5100} , but plausibly with a time delay. Using the same procedure for computing H β lags, we determine the lag of R_{BLR} with respect to \bar{L}_{5100} : $\tau_{R-\bar{L}} = 2.35^{+3.47}_{-1.25}$ yrs. From analysis of the CCCD and CCPD, the probability of $\tau_{R-\bar{L}} \leq 0$ yrs $p = 0.06$ and 0.098 , respectively, suggesting that there may be a potential delay between R_{BLR} and \bar{L}_{5100} . Clearly, we need more RM monitoring campaigns to verify this intriguing, but tentative result.

There are two timescales for the ionized clouds in the BLR. The recombination timescale is $t_{\text{rec}} = (n_e \alpha_B)^{-1} = 6.0 n_{10}^{-1} \text{ min}$, where $n_{10} = n_e/10^{10} \text{ cm}^{-3}$ is the electron density of the clouds and α_B is the case B recombination coefficient (Osterbrock 1989). The fast response of the ionization front exactly follows the ionizing luminosity, as shown by Equation (6). However, radiation pressure, if effective, drives the clouds to outwards, changes their orbits, and leads to variations of their spatial distribution. The observed size of the BLR is actually an emissivity-averaged value over the whole BLR, namely $R_{\text{BLR}} = \int R \epsilon dR / \int \epsilon dR$, where ϵ is the emissivity of the clouds, determined by their

spatial distribution (or, equivalently, their number density). Radiation pressure induces changes in ϵ , and thereby R_{BLR} . Considering that the $\text{H}\beta$ line width represents the bulk motion of the clouds, the dynamical timescale of the BLR is given by (Peterson 1993)

$$t_{\text{BLR}} = \frac{c\tau_{\text{H}\beta}}{V_{\text{FWHM}}} = 3.36 \tau_{20} V_{5000}^{-1} \text{ yrs}, \quad (9)$$

where $V_{5000} = V_{\text{FWHM}}/5000 \text{ km s}^{-1}$ and $\tau_{20} = \tau_{\text{H}\beta}/20$ days. The quantity t_{BLR} represents the typical timescale with which R_{BLR} varies in response to a change in the BLR dynamics. For NGC 5548, the average $\text{H}\beta$ lag of $\tau_{\text{H}\beta} = 15$ days and line width of $V_{\text{FWHM}} = 6000 \text{ km s}^{-1}$ leads to a dynamical timescale of $t_{\text{BLR}} \approx 2.10 \text{ yrs}$.

Interestingly, $t_{\text{BLR}} \approx \tau_{R-\bar{L}}$, indicating that the BLR could be jointly controlled by radiation pressure and BH gravity. A mass inflow to the center can give rise to variations of the BLR and the accretion disk, but changes in the BLR structure (size) should precede changes in the disk luminosity. The delayed response of the BLR size to continuum luminosity may rule out this possibility, plausibly implicating the potential role of radiation pressure.

6. Conclusions

We present results of a new RM campaign on NGC 5548 based on high-quality optical spectra taken in 2015. We measure a centroid time lag for the broad $\text{H}\beta$ line of $\tau_{\text{H}\beta} = 7.20^{+1.33}_{-0.35}$ days in the rest frame. Adopting a virial factor of $f_{\text{BLR}} = 6.3 \pm 1.5$ and an $\text{H}\beta$ line dispersion of $\sigma_{\text{line}} = 3124 \pm 302 \text{ km s}^{-1}$, we measured a BH mass of $M_{\bullet} = 8.71^{+3.21}_{-2.61} \times 10^7 M_{\odot}$. We obtain the following results:

- The velocity-resolved delay map of the broad $\text{H}\beta$ line shows a symmetric structure, consistent with the previous results of Denney et al. (2009b).
- The relation between $\text{H}\beta$ line width and $\text{H}\beta$ time lag is consistent with virial motions. The virial product varies weakly with luminosity but is largely constant.
- The BLR size of NGC 5548 follows $R_{\text{H}\beta} \propto L_{5100}^{0.86}$, steeper than the slope of ~ 0.5 for the global $R_{\text{H}\beta} - L_{5100}$ relation for all RM AGNs.
- Examining the variation patterns of R_{BLR} and \bar{L}_{5100} , we find tentative evidence that R_{BLR} follows \bar{L}_{5100} with a delay of $2.35^{+3.47}_{-1.25} \text{ yrs}$. This is consistent with the dynamical timescale of the BLR, implying that the long-term variations of the BLR may be driven by radiation pressure.

We are grateful to the referee for a helpful report. We acknowledge the support of the staff of the Lijiang 2.4m telescope. Funding for the telescope has been provided by CAS and the People's Government of Yunnan Province. This research is supported by the Strategic Priority Research

Program - The Emergence of Cosmological Structures of the Chinese Academy of Sciences, Grant No. XDB09000000, by NSFC grants NSFC-11173023, -11133006, -11373024, -11273007 -11233003, -11573026, -11503026 and -11473002, and a NSFC-CAS joint key grant U1431228.

REFERENCES

- Ade, P. A. R., Arnaud, M., et al. (Planck Collaboration) 2014, *A&A*, 571, A31
- Alexander, T. 1997, *Astronomical Time Series*, eds. D. Maoz, A. Sternberg & E.M. Leibowitz, Kluwer, Dordrecht, p. 163
- Bahcall, J. N., Kozlovsky, B.-Z., & Salpeter, E. E. 1972, *ApJ*, 171, 467
- Bentz, M. C., Denney, K. D., Grier, C. J., et al. 2013, *ApJ*, 767, 149
- Bentz, M. C., Horne, K., Barth, A. J., et al. 2010, *ApJ*, 720, L46
- Bentz, M. C., Walsh, J. L., Barth, A. J., et al. 2009, *ApJ*, 705, 199
- Bentz, M. C., Walsh, J. L., Barth, A. J., et al. 2008, *ApJ*, 689, L21
- Bentz, M. C., Denney, K. D., Cackett, E. M., et al. 2007, *ApJ*, 662, 205
- Blandford, R. D., & McKee, C. F. 1982, *ApJ*, 255, 419
- Boroson, T. A., & Green, R. F. 1992, *ApJS*, 80, 109
- Bruzual, G., & Charlot, S. 2003, *MNRAS*, 344, 1000
- Chiang, J. & Blaes, O. 2003, *ApJ*, 586, 97
- Collin, S., Kawaguchi, T., Peterson, B. M., & Vestergaard, M. 2006, *A&A*, 456, 75
- Denney, K. D., Peterson, B. M., Pogge, R. W., et al. 2010, *ApJ*, 721, 715
- Denney, K. D., Watson, L. C., Peterson, B. M., et al. 2009a, *ApJ*, 702, 1353
- Denney, K. D., Peterson, B. M., Pogge, R. W., et al. 2009b, *ApJ*, 704, L80
- De Rosa, G., Peterson, B. M., Ely, J., et al. 2015, *ApJ*, 806, 128
- Du, P., Lu, K.-X., Hu, C., et al. 2016, *ApJ*, submitted
- Du, P., Lu, K.-X., Hu, C., et al. 2016, *ApJ*, 820, 27
- Du, P., Hu, C., Lu, K.-X., et al. 2015, *ApJ*, 806, 22
- Du, P., Hu, C., Lu, K.-X., et al. 2014, *ApJ*, 782, 45

- Edelson, R., Gelbord, J. M., Horne, K., et al. 2015, *ApJ*, 806, 129
- Edelson, R., Turner, T. J., Pounds, K., et al. 2002, *ApJ*, 568, 610
- Edelson, R. A., & Krolik, J. H. 1988, *ApJ*, 333, 646
- Fausnaugh, M. M., Denney, K. D., Barth, A. J., et al. 2015, [arXiv:1510.05648](#)
- Filippenko, A. 1982, *PASP*, 94, 715
- Gaskell, C. M., & Peterson, B. M. 1987, *ApJS*, 65, 1
- Gaskell, C. M., & Sparke, L. S. 1986, *ApJ*, 305, 175
- Grier, C. J., Peterson, B. M., Horne, K., et al. 2013, *ApJ*, 764, 47
- Ho, L. C., & Kim, M. 2014, *ApJ*, 789, 17
- Hu, C., Du, P., Lu, K.-X., et al. 2015, *ApJ*, 804, 138
- Kaspi, S., Smith, P. S., Netzer, H., et al. 2000, *ApJ*, 533, 631
- Kaspi, S., Maoz, D., Netzer, H., et al. 2005, *ApJ*, 629, 61
- Kilerci Eser, E., Vestergaard, M., Peterson, B. M., et al. 2015, *ApJ*, 801, 8
- Kollatschny, W. & Zetzl, M. 2013, *A&A*, 549, A100
- Kormendy, J., & Ho, L. C. 2013, *ARA&A*, 51, 511
- Li, Y.-R., Wang, J.-M., Ho, L. C., Du, P., & Bai, J.-M. 2013, *ApJ*, 779, 110
- Li, Y.-R., Wang, J.-M., Ho, L. C., et al. 2016, *ApJ* in press ([arXiv:1602.05005](#))
- Maoz, D., Netzer, H., Leibowitz, E., et al. 1990, *ApJ*, 351, 75
- Onken, C. A., Ferrarese, L., Merritt, D., et al. 2004, *ApJ*, 615, 645
- Osterbrock, D. E. 1989, *Astrophysics of Gaseous Nebulae and Active Galactic Nuclei* (Mill Valley, University Science Books)
- Pancoast, A., Brewer, B. J. & Treu, T. 2011, *ApJ*, 730, 139
- Pancoast, A., Brewer, B. J., & Treu, T. 2014a, *MNRAS*, 445, 3055
- Pancoast, A., Brewer, B. J., Treu, T., et al. 2014b, *MNRAS*, 445, 3073
- Peterson, B. 1993, *PASP*, 105, 247
- Peterson, B. M., Ferrarese, L., Gilbert, K. M., et al. 2004, *ApJ*, 613, 682

- Peterson, B. M., Berlind, P., Bertram, R., et al. 2002, *ApJ*, 581, 197
- Peterson, B. M., Barth, A. J., Berlind, P., et al. 1999, *ApJ*, 510, 659
- Peterson, B. M., Wanders, I., Horne, K., et al. 1998, *PASP*, 110, 660
- Press, W. H., Teukolsky, S. A., Vetterling, W. T., & Flannery, B. P. 1992, *Numerical Recipes in FORTRAN* (2nd ed.; Cambridge: Cambridge Univ. Press)
- Rodríguez-Pascual, P. M., Alloin, D., Clavel, J., et al. 1997, *ApJS*, 110, 9
- Sergeev, S. G., Doroshenko, V. T., Dzyuba, S. A., et al. 2007, *ApJ*, 668, 708
- Shakura, N. I. & Sunyaev, R. A. 1973, *A&A*, 24, 337
- Vasudevan, R. V., & Fabian, A. C. 2009a, *MNRAS*, 392, 1124
- Vasudevan, R. V., Mushotzky, R. F., Winter, L. M., & Fabian, A. C. 2009b, *MNRAS*, 399, 1553
- Vasudevan, R. V., Fabian, A. C., Gandhi, P., Winter, L. M., & Mushotzky, R. F. 2010, *MNRAS*, 402, 1081
- Wanders, I., & Peterson, B. M. 1996, *ApJ*, 466, 174
- White, R. J., & Peterson, B. M. 1994, *PASP*, 106, 879
- Woo, J.-H., Treu, T., Barth, A. J., et al. 2010, *ApJ*, 716, 269

A. Mean and RMS Spectra

The standard definitions of mean and RMS spectra are given by (Peterson et al. 2004)

$$\bar{F}_\lambda = \frac{1}{N} \sum_{i=1}^N F_i(\lambda) \quad (\text{A1})$$

and

$$S_\lambda = \left\{ \frac{1}{N} \sum_{i=1}^N [F_i(\lambda) - \bar{F}(\lambda)]^2 \right\}^{1/2}, \quad (\text{A2})$$

where $F_i(\lambda)$ is the i -th spectrum and N is the total number of spectra obtained during the campaign. We calculated the mean and RMS spectra of NGC 5548 from all the spectra with absolute flux calibration and show them in Figure 10. The line dispersion is calculated as

$$\sigma_{\text{line}}^2(\lambda) = \langle \lambda^2 \rangle - \lambda_0^2, \quad (\text{A3})$$

where $\lambda_0 = \int \lambda P(\lambda) d\lambda / \int P(\lambda) d\lambda$, $\langle \lambda^2 \rangle = \int \lambda^2 P(\lambda) d\lambda / \int P(\lambda) d\lambda$, and $P(\lambda)$ is the line profile.

Table 1. Continuum and $H\beta$ fluxes for NGC 5548

JD –2450000	F_{5100}	$F_{H\beta}$	JD –2450000	V–band (mag)
7030.50	5.46 ± 0.29	8.00 ± 0.24	7030.50	1.38 ± 0.05
7037.50	4.96 ± 0.29	7.96 ± 0.24	7037.50	1.45 ± 0.01
7043.50	5.67 ± 0.33	7.89 ± 0.27	7044.50	1.45 ± 0.01
7047.50	4.65 ± 0.32	7.78 ± 0.26	7046.50	1.44 ± 0.01
7055.50	4.17 ± 0.28	7.84 ± 0.24	7047.50	1.46 ± 0.01

Note. — F_{5100} is the flux density at 5100 Å in units of $10^{-15} \text{erg s}^{-1} \text{cm}^{-2} \text{Å}^{-1}$ and $F_{H\beta}$ is the $H\beta$ flux in units of $10^{-13} \text{erg s}^{-1} \text{cm}^{-2}$. (This table is available in its entirety in a machine-readable form in the online journal. A portion is shown here for guidance regarding its form and content.)

Table 2. Statistics of Light Curves for NGC 5548 in 2015

Time Series	N	$\langle T \rangle$ (days)	T_{median} (days)	Mean Flux ^a	F_{var}	R_{max}
(1)	(2)	(3)	(4)	(5)	(6)	(7)
5100 Å	62	3.4	3.0	4.34 ± 0.30	0.23 ± 0.02	2.31
$H\beta$	62	3.4	3.0	6.95 ± 0.25	0.10 ± 0.01	1.52

Note. — Col. (1) is time series. Col. (2) is the number of data points. Cols. (3) and (4) are the mean and median sampling intervals, respectively. Col. (5) is the mean flux and standard deviation. Cols. (6) and (7) are F_{var} and R_{max} defined in Section 3.1.

^a The units of F_{5100} and $F_{H\beta}$ are the same as in Table 1.

Table 3. RM Measurements

Parameter	Value
τ_{cent} ($H\beta$ vs. F_{5100})	$7.20^{+1.33}_{-0.35}$ days
τ_{peak} ($H\beta$ vs. F_{5100})	$7.18^{+1.38}_{-0.70}$ days
FWHM (RMS)	$9450 \pm 290 \text{ km s}^{-1}$
σ_{line} (RMS)	$3124 \pm 302 \text{ km s}^{-1}$
FWHM (mean)	$9912 \pm 362 \text{ km s}^{-1}$
σ_{line} (mean)	$3350 \pm 272 \text{ km s}^{-1}$
$\log(\bar{L}_{5100}/\text{erg s}^{-1})$	43.21 ± 0.12
$\log(\bar{L}_{H\beta}/\text{erg s}^{-1})$	41.70 ± 0.05

Note. — τ_{cent} and τ_{peak} are given in the rest-frame.

Table 4. All the RM measurements of NGC 5548

Data Set	Observation Epoch	T (Year)	F_{var}	$\log \bar{L}_{5100}$ (erg s $^{-1}$)	$\log \bar{L}_{\text{H}\beta}$ (erg s $^{-1}$)	$\text{H}\beta$ lags (days)	Mean spectra		RMS spectra		$\log M_{\bullet}$ (M_{\odot})	Ref.
							FWHM (km s $^{-1}$)	σ_{line} (km s $^{-1}$)	FWHM (km s $^{-1}$)	σ_{line} (km s $^{-1}$)		
(1)	(2)	(3)	(4)	(5)	(6)	(7)	(8)	(9)	(10)	(11)	(12)	(13)
Year 1	1988 Dec–1989 Oct	1989.55	0.188	43.39 ± 0.09	41.76 ± 0.04	$19.70^{+1.50}_{-1.50}$	4674 ± 63	1934 ± 5	4044 ± 199	1687 ± 56	$7.84^{+0.11}_{-0.11}$	1,2,3
Year 2	1989 Dec–1990 Oct	1990.55	0.272	43.13 ± 0.10	41.61 ± 0.05	$18.60^{+2.10}_{-2.30}$	5418 ± 107	2223 ± 20	4664 ± 324	1882 ± 83	$7.91^{+0.12}_{-0.12}$	1,2,3
Year 3	1990 Nov–1991 Oct	1991.45	0.154	43.32 ± 0.09	41.69 ± 0.06	$15.90^{+2.90}_{-2.50}$	5236 ± 87	2205 ± 16	5776 ± 237	2075 ± 81	$7.93^{+0.13}_{-0.13}$	1,2,3
Year 4	1992 Jan–1992 Oct	1992.65	0.386	43.06 ± 0.10	41.48 ± 0.05	$11.00^{+1.90}_{-2.00}$	5986 ± 95	3109 ± 53	5691 ± 164	2264 ± 88	$7.84^{+0.13}_{-0.13}$	1,2,3
Year 5	1992 Nov–1993 Sep	1993.45	0.148	43.33 ± 0.09	41.73 ± 0.06	$13.00^{+1.40}_{-1.40}$	5930 ± 42	2486 ± 13	—	1909 ± 129	$7.77^{+0.13}_{-0.13}$	1,2,3
Year 6	1993 Nov–1994 Oct	1994.45	0.173	43.35 ± 0.09	41.69 ± 0.04	$13.40^{+3.80}_{-4.30}$	7378 ± 39	2877 ± 17	7202 ± 392	2895 ± 114	$8.14^{+0.16}_{-0.18}$	1,2,3
Year 7	1994 Nov–1995 Oct	1995.45	0.117	43.50 ± 0.08	41.80 ± 0.04	$21.70^{+2.60}_{-2.60}$	6946 ± 79	2432 ± 13	6142 ± 289	2247 ± 134	$8.13^{+0.13}_{-0.13}$	1,2,3
Year 8	1995 Nov–1996 Oct	1996.45	0.244	43.38 ± 0.08	41.73 ± 0.04	$16.40^{+1.20}_{-1.10}$	6623 ± 93	2276 ± 15	5706 ± 357	2026 ± 68	$7.92^{+0.11}_{-0.11}$	1,2,3
Year 9	1996 Dec–1997 Oct	1997.55	0.209	43.17 ± 0.09	41.67 ± 0.09	$17.50^{+2.00}_{-1.60}$	6298 ± 65	2178 ± 12	5541 ± 354	1923 ± 62	$7.90^{+0.12}_{-0.11}$	1,2,3
Year 10	1997 Nov–1998 Sep	1998.45	0.146	43.52 ± 0.08	41.86 ± 0.03	$26.50^{+4.30}_{-2.20}$	6177 ± 36	2035 ± 11	4596 ± 505	1732 ± 76	$7.99^{+0.13}_{-0.12}$	1,2,3
Year 11	1998 Nov–1999 Oct	1999.55	0.229	43.44 ± 0.08	41.76 ± 0.06	$24.80^{+3.20}_{-3.00}$	6247 ± 57	2021 ± 18	6377 ± 147	1980 ± 30	$8.08^{+0.12}_{-0.12}$	1,2,3
Year 12	1999 Dec–2000 Sep	2000.45	0.424	42.98 ± 0.11	41.57 ± 0.04	$6.50^{+5.70}_{-3.70}$	6240 ± 77	2010 ± 30	5957 ± 224	1969 ± 48	$7.49^{+0.40}_{-0.27}$	1,2,3 ^a
Year 13	2000 Nov–2001 Dec	2001.45	0.293	42.96 ± 0.11	41.46 ± 0.05	$14.30^{+5.90}_{-7.30}$	6478 ± 108	3111 ± 131	6247 ± 343	2173 ± 89	$7.92^{+0.21}_{-0.17}$	1,2,3
Year 17	2005 Mar–2005 Apr	2005.35	0.187	42.59 ± 0.20	41.07 ± 0.09	$6.30^{+2.60}_{-2.30}$	6396 ± 167	3210 ± 642	—	2939 ± 768	$7.83^{+0.23}_{-0.22}$	1,4
Year 19	2007 Mar–2007 Jul	2007.55	0.157	42.73 ± 0.15	41.19 ± 0.10	$12.40^{+2.74}_{-3.85}$	11481 ± 574	—	4849 ± 112	1822 ± 35	$7.70^{+0.14}_{-0.14}$	1,5
Year 20	2008 Feb–2008 Jun	2008.35	0.227	42.68 ± 0.14	41.21 ± 0.06	$4.17^{+0.90}_{-1.33}$	12771 ± 71	4266 ± 65	11177 ± 2266	4270 ± 292	$7.97^{+0.15}_{-0.18}$	1,6 ^b
Year 25	2013 Dec–2014 Aug	2014.45	—	43.22 ± 0.14	—	$8.57^{+0.67}_{-0.67}$	—	—	—	—	—	7
Year 26	2015 Jan–2015 Jul	2015.45	0.233	43.21 ± 0.12	41.70 ± 0.05	$7.20^{+1.33}_{-0.35}$	9912 ± 362	3350 ± 272	9450 ± 290	3124 ± 302	$7.94^{+0.16}_{-0.13}$	8

Note. — M_{\bullet} is calculated from the line dispersion of the RMS spectrum with a virial factor of $f_{\text{BLR}} = 6.3 \pm 1.5$ (Ho & Kim 2014). These campaigns yield a mean BH mass of $\langle M_{\bullet} \rangle = (8.39 \pm 0.72) \times 10^7 M_{\odot}$.

^a “Year 12” is compiled from the 12th RM observation in the AGN Watch project (Peterson et al. 2002). The cross-correlation analysis is very ambiguous (see Figure 2 of Peterson et al. 2002), and we excluded this data set in our analysis.

^b Pancoast et al. (2014b) modelled the data and provided the model-dependent $\text{H}\beta$ lag of $3.22^{+0.66}_{-0.54}$ days, which is consistent (within the uncertainties) with $4.17^{+0.90}_{-1.33}$ days determined by the cross correlation analysis in Bentz et al. (2010). We use the $\text{H}\beta$ lag of Bentz et al. (2010) for consistency.

References. (1) Kilerci Eser et al. (2015), (2) Collin et al. (2006), (3) Peterson et al. (2004), (4) Bentz et al. (2007), (5) Denney et al. (2010), (6) Bentz et al. (2010), (7) Fausnaugh et al. (2015), (8) This work.

Table 5. Simultaneous Observations of the Spectral Energy Distribution for NGC 5548

References	Observations	$\log (L_{\text{bol}}/\text{erg s}^{-1})$	ϵ_{Edd}	Notes
V09a	XMM(OM, EPIC-pn) in Dec. 2000	44.35 ± 0.04	0.018 ± 0.002	simultaneous
V09b	Swift(UVOT, XRT) in Jul. 2007	44.15 ± 0.04	0.011 ± 0.002	simultaneous
V10	Swift(BAT) in Jul. 2007, IRAS in 1983	44.50 ± 0.04	0.025 ± 0.003	not simultaneous

Note. — **References:** V09a: [Vasudevan & Fabian \(2009a\)](#); V09b: [Vasudevan et al. \(2009b\)](#); V10: [Vasudevan et al. \(2010\)](#).

There are many observations of NGC 5548 (see [Chiang & Blaes 2003](#) for a brief summary of data). Here we only list the recent observations. “Simultaneous” means that the UV, optical, and X-ray data are simultaneously observed.

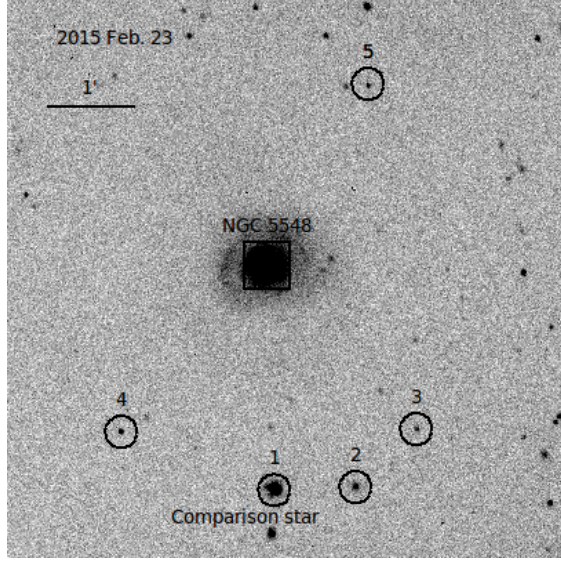


Fig. 1.— Johnson *V*-band image of NGC 5548 from the Lijiang 2.4m telescope, observed on February 23, 2015. NGC 5548 is located in the center of the field. Stars 1–5 are selected as photometric comparison stars, and star 1 is selected as the spectral comparison star.

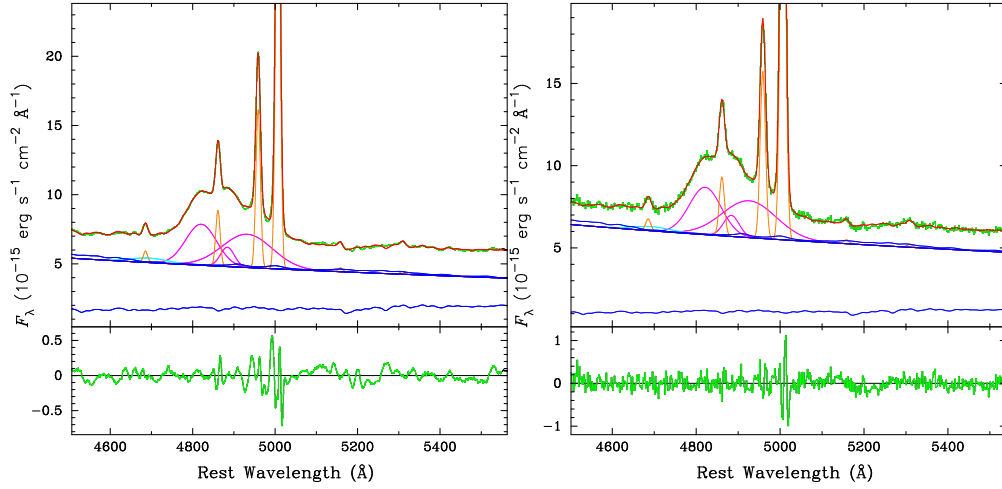


Fig. 2.— Multi-components fitting of (*left*) the mean spectrum and (*right*) an individual spectrum of NGC 5548. The trace shows the spectrum corrected for Galactic extinction (green) and the best-fit model (red), which is composed of the AGN power-law continuum (blue), Fe II emission lines (blue; template from Boroson & Green 1992), host galaxy (blue), broad H β (magenta), broad He II λ 4686 (cyan), and several narrow emission lines (orange). The bottom trace shows the residuals.

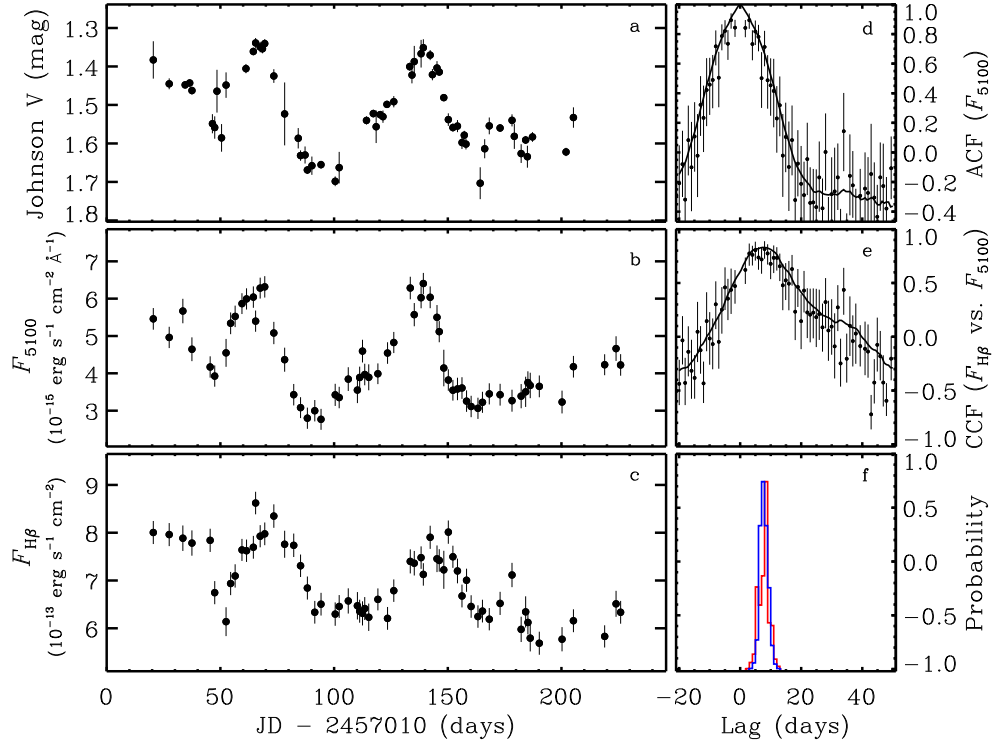


Fig. 3.— Light curves and the results of cross correlation analysis. Panels (*d*, *e*, *f*) are the ACF of continuum at 5100 Å, CCF between the H β emission line and continuum at 5100 Å, and the Monte Carlo simulations of peak (red) and centroid (blue) of lags, respectively. In panels (*d*, *e*), the solid lines show the ICCF, and points with error bars show the ZDCF. The light curves in panels (*b*, *c*) include the systematic uncertainties.

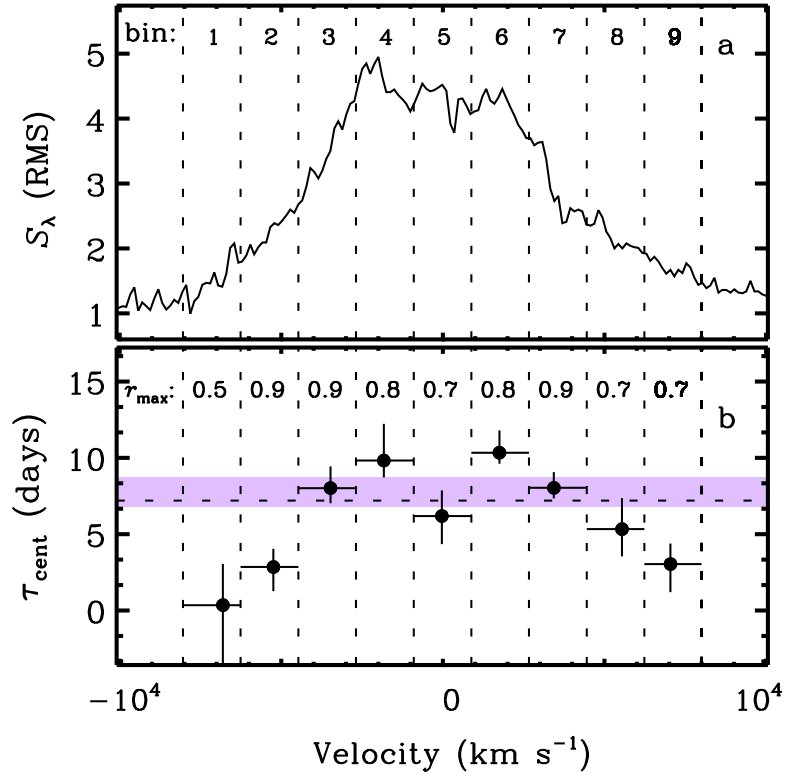


Fig. 4.— Panel (a) shows the RMS spectra of $\text{H}\beta$. We divided the profile into 9 bins. Panel (b) shows the centroid lags of each $\text{H}\beta$ bin. The vertical dash-lines are the edges of bins, and the black horizontal dashed line with purple shaded area shows the average time lag with uncertainties.

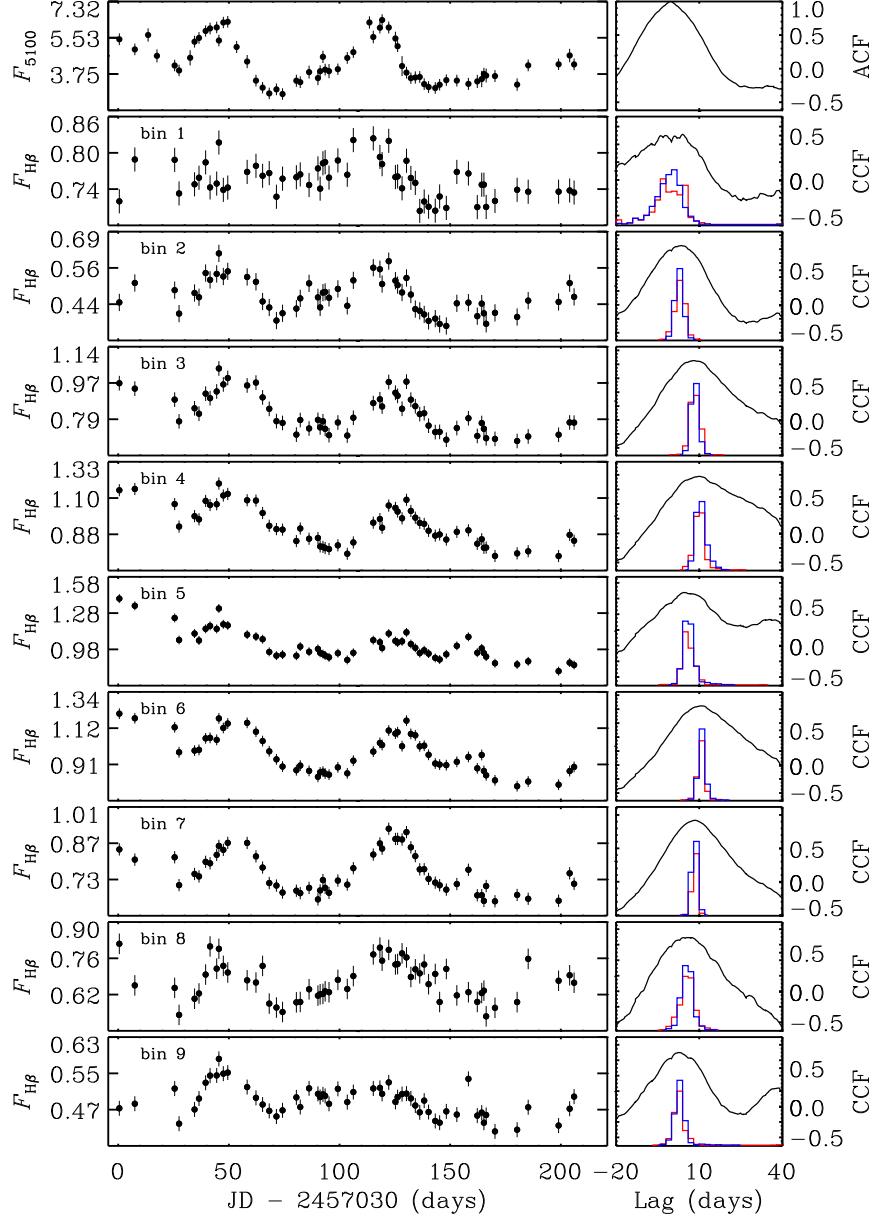


Fig. 5.— Velocity-resolved reverberation mapping. The left panels show the light curves of continuum at 5100 Å, and Hβ emission line of each velocity bin, respectively. We divided the Hβ profile into 9 velocity bins and numbered each bin from 1 to 9. The right panels correspond to the ACF of continuum and the CCF between the light curve of each bin and continuum, respectively. Monte Carlo simulations of the peaks (red) and centroid (blue) of time lags are overplotted in the CCF panels.

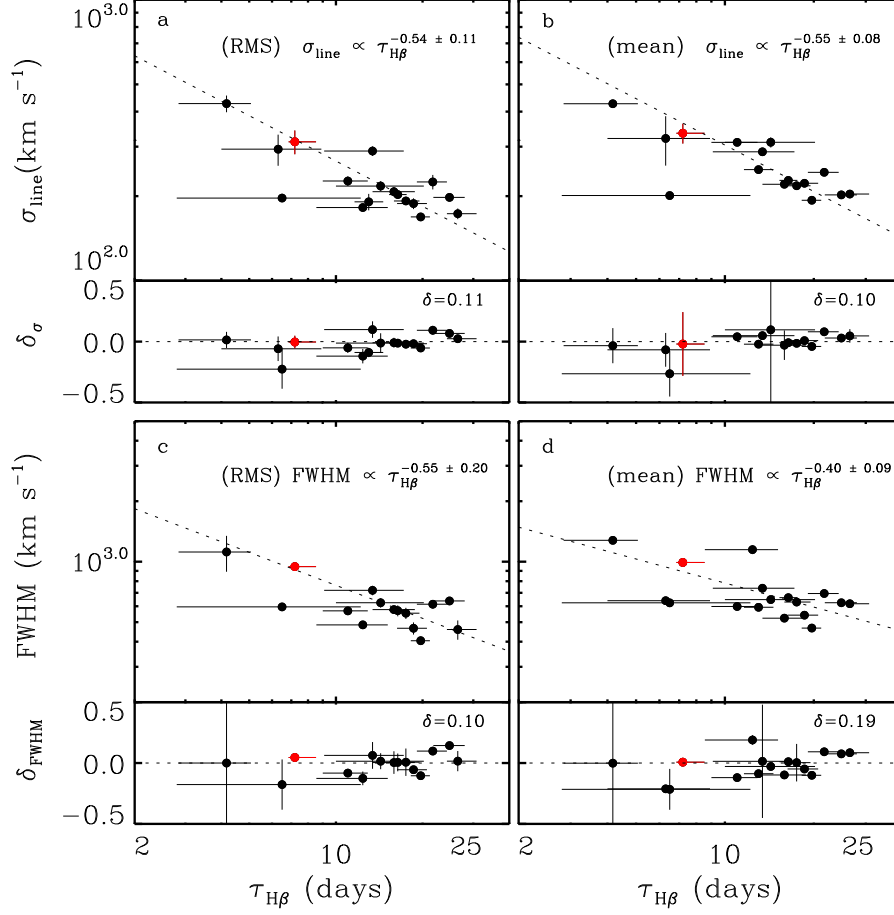


Fig. 6.— The dependence of H β line dispersion and FWHM on H β lag for mean and RMS spectra of NGC 5548. The bottom panel of each plot shows the residuals from the virial relation. The inset value of δ shows the deviation of the BLR motion from the virial relation, defined by Equation (4). The red point is from the present work.

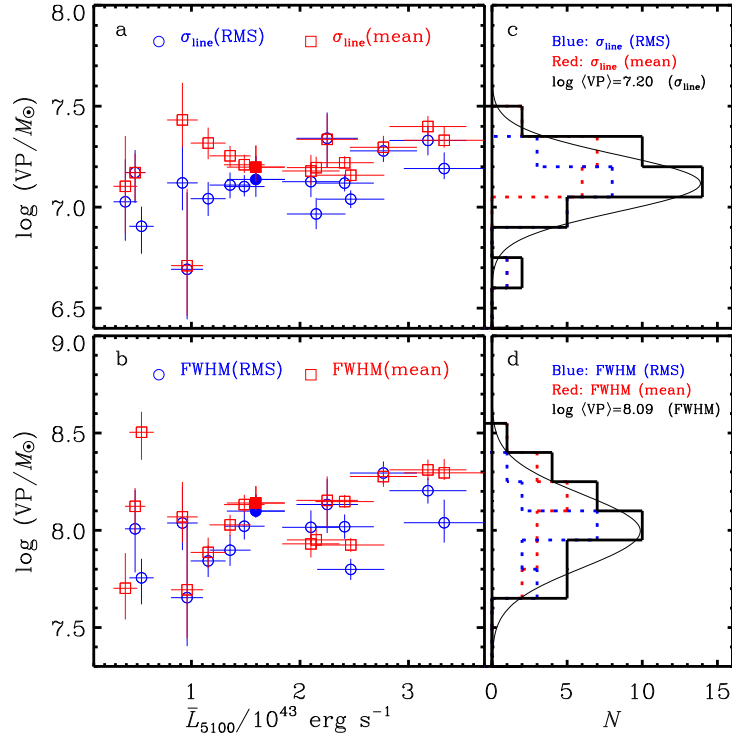


Fig. 7.— The virial product (VP) vs. the optical luminosity (corrected for the starlight contribution of host galaxy). In panels (a, b), the solid points are from this work and the open symbols are from previous RM measurements. Panels (c, d) show the corresponding distributions of VP, fit with a Gaussian (solid line).

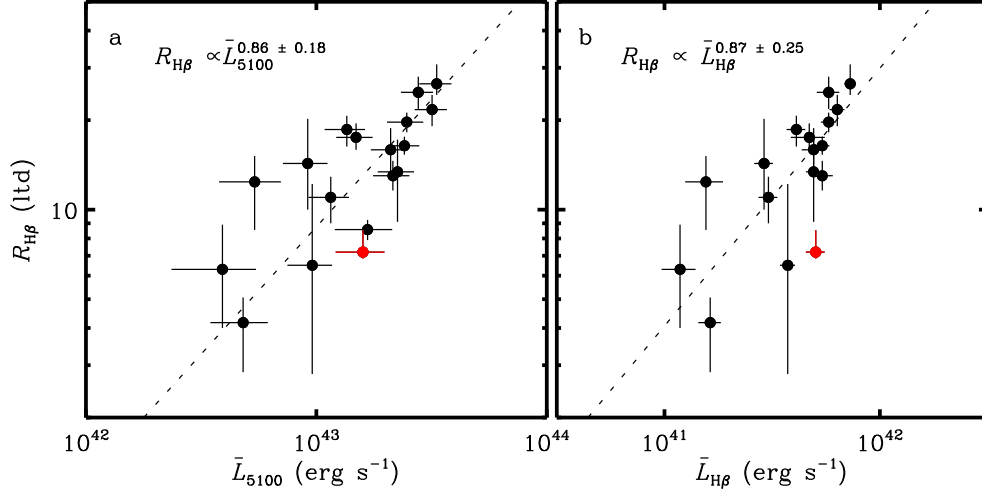


Fig. 8.— The (a) $R_{H\beta} - \bar{L}_{5100}$ and (b) $R_{H\beta} - \bar{L}_{H\beta}$ relation of NGC 5548. The red point is from this work, and the black points are from previous RM measurements.

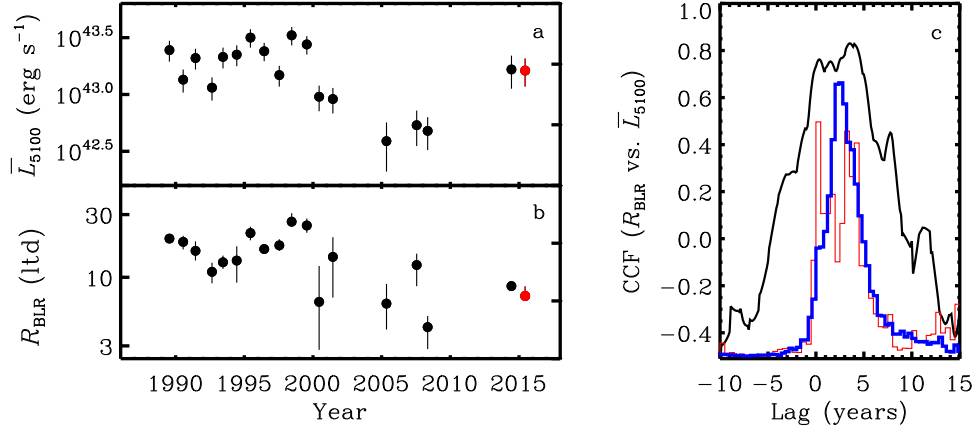


Fig. 9.— The secular variations of epoch-averaged (a) optical luminosity, \bar{L}_{5100} , and (b) BLR size, R_{BLR} . The red point is from the present campaign. Panel (c) shows the CCF of R_{BLR} with respect to \bar{L}_{5100} and the distributions of Monte Carlo simulations of the centroid (blue) and peak (red) lags.

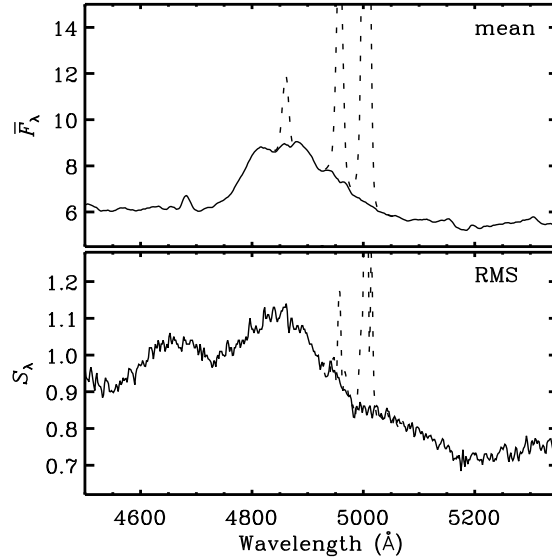


Fig. 10.— The mean (\bar{F}_λ) and RMS (S_λ) spectrum in units of $10^{-15} \text{ erg s}^{-1} \text{ cm}^{-2} \text{ \AA}^{-1}$ (solid line). The dash line represents the components of narrow emission lines.